Article

Improving the Modeling of Pressure Pulsation and Cavitation Prediction in a Double-Volute Double-Suction Pump Using Mosaic Meshing Technology

Virgel M. Arocena [ID] and Louis Angelo M. Danao *[ID]

Department of Mechanical Engineering, University of the Philippines Diliman, Quezon City 1101, Philippines
* Correspondence: louisdanao@up.edu.ph

Abstract: Over the years, Computational Fluid Dynamics (CFD) has been an integral part of most pump design processes. Unfortunately, as calculation schemes and flow investigations become more complicated, the cost of conducting numerical simulations also becomes more expensive in terms of computational time. To remedy this, cutting-edge technology, together with novel calculation techniques, are continuously introduced with the end target of producing more accurate results and faster computing time. In this paper, CFD simulations are run on a numerical model of a double-volute double-suction pump prepared using ANSYS Fluent Mosaic meshing technology. Poly-Hexcore, the first application of Mosaic technology, fills the bulk region with octree hexes, keeps a high-quality layered poly-prism mesh in the boundary layer, and conformally connects these two meshes with general polyhedral elements. This technology promises to provide a lower number of cells along with a significant increase in computing speed. In this paper, steady state results of the model with Mosaic Poly-Hexcore mesh with ~37% fewer cells produced comparable results with a similarly sized model prepared with multi-block structured hexagonal mesh. The predicted pump head, efficiency and shaft power under the design conditions were within 1% for both models, while calculation time was reduced by ~25%. Additional simulations using the Poly-Hexcore mesh showed that the model was able to closely predict the pump's NPSH3 for $0.8Q_D$, $1.0Q_D$, and $1.2Q_D$ compared with the manufacturer's data. Under cavitating flow conditions, the formation of vapor bubbles was observed on the suction side, starting at the leading edge of the blade and slowly forming as thin sheets towards the trailing edge as the suction pressure is reduced. Lastly, pressure fluctuations were observed from pressure coefficient data collected at several monitoring points in the volute and the impeller. It was seen that due to the interaction between the stationary casing and the rotating impeller, pulsations were equivalent to the blade passing frequency and its harmonics.

Keywords: cavitation; CFD; double-volute pump; NPSH

1. Introduction

Centrifugal pumps are one of the most widely used mechanical equipment found in various industries. They are an integral part of almost all process applications and are expected to operate continuously and with a high level of reliability. The basic design of a centrifugal pump consists of a principal element called a bladed impeller which, due to its rotational motion, imparts kinetic and potential energy to the fluid. This energy is then converted into useable pressure directing flow into the diffuser or the discharge volute. Although the operating principle may be straightforward, flows within rotodynamic pumps are three-dimensional, unsteady, and extremely complex. In the impeller region alone, there are four secondary flow mechanisms caused by the meridional curvature, rotational effects, blade forces, and the axial flow or flow parallel to the axis of the pump shaft as the fluid enters the impeller [1]. Within the pump, low-pressure regions on the surface of the impellers are usually or almost always created, which encourages the formation of

vapor bubbles. The rapid formation, growth and collapse of these vapor bubbles can lead to cavitation resulting in performance degradation, vibration, noise, structural damage, and even catastrophic failure. Aside from this condition, studies show that geometric parameters such as cutwater gap, impeller width and diameter, number of blades, casing shape, etc., also influence pump performance. Examples are those published by Zhang [2] et al. and Luo et al. [3], which showed that parameters such as the impeller inlet diameter, blade inlet angle, and inlet blade thickness are crucial in improving both the hydraulic and cavitation performance of a centrifugal pump. Similarly, flow conditions such as flow rate, rotating speed, and suction condition, either by themselves or combined with geometric parameters, have been observed to have a significant effect on pump performance. Up to a certain point, head and efficiency have been shown to increase simultaneously with an increase in rotational speed and the number of blades [4,5]. However, it is important to note that depending on the type of application, there will always be a maximum value on the number of blades which can guarantee an increase in efficiency. Beyond this optimum point, the high blade count will serve as an obstruction choking the flow and increasing frictional losses. At this point, performance will begin to degrade. On the other hand, pressure fluctuations were observed to vary inversely with flow rate. Lower values were observed at the design flow rate and higher at off-design flow rates. Additionally, pressure fluctuations decreased appreciably as the rotational speed was reduced from the rated speed, with the maximum pump efficiency remaining unchanged [6].

Traditionally, designers and fluid engineers have access to numerous guidelines and standards which they can use in designing pumps, all of which ensure consistent and safe pump design, manufacturing, and operation while ensuring efficiency—at least to some extent. Ultimately, to guarantee optimum pump performance, physical model tests and experiments are necessary for some, if not most, applications. Unfortunately, financial and time constraints sometimes impose restrictions on conducting physical model tests. These constraints limit the possibility of conducting in-depth investigations or finding innovative ways of designing new and more reliable pumps. On the other hand, through developments and advances in computer technology, design engineers can have a better understanding of the flow phenomena within the pump using numerical simulations. Recent progress in CFD provides designers the capability to predict complex three-dimensional viscous flow, cavitation, and flow instabilities, among others. Serving as tools that help the designers and fluid engineers in addressing the end-users' requirement for more energy-efficient and more reliable pumps. Additionally, the number of research and studies highlighting the physics of the flow within the pump using CFD is continuously increasing. Early adopters include the works made by Chen and Liaw [7] on the effect of the volute casing on the flow field within the pump. Their study highlighted a significant fluctuation in the flow, especially while the trailing edge of the impeller is passing the volute tongue. Morgut and Nobile [8] evaluated the accuracy of numerical predictions of cavitating flows on scaled model propellers for marine applications. Their study showed that numerical predictions for both partial and tip vortex cavitation compared well with experimental data. However, a slight tendency to overestimate the cavity growth was also observed. Further studies extending the capability to predict cavitation in centrifugal pumps include the works of Liu et al. [9]. The authors applied the modified k-ω turbulence model and the Schnerr-Sauer [10] cavitation model in ANSYS CFX in predicting cavitating flow in a centrifugal pump. Cavitation growth was observed starting from the leading edge of the suction side of the blades and expanding towards the trailing edge as the cavitation number decreased. Works similar to those done by Jafarzadeh et al. [11] showed that characteristic curves obtained through CFD are in acceptable agreement with experimental data.

As CFD codes continue to improve, the role it has in pump development continues to expand. Unfortunately, as calculation schemes and flow investigations become more complicated, the cost of conducting numerical simulations also becomes more expensive in terms of computational time. To remedy this, cutting-edge technology, together with novel calculation techniques, are continuously introduced with the end target of producing more

accurate results and faster computing time. In this paper, CFD simulations for a double-volute double-suction pump were run using ANSYS Fluent 2022 R2. The mesh for the computational domain is prepared using the software's new Mosaic meshing technology. Poly-Hexcore, the first application of Mosaic technology, fills the bulk region with octree hexes, keeps a high-quality layered poly-prism mesh in the boundary layer, and conformally connects these two meshes with general polyhedral elements [12]. This innovative meshing technique reduces mesh count by as much as 46% compared to Hexcore with tetrahedral elements and promises gains in calculation speed between 20% to 50% depending on the type of application [12,13]. Additionally, to avoid the tedious trial-and-error process in predicting required NPSH, the novel approach proposed by Ding et al. [14] was tested in this paper. The study aims to compare calculation results against the manufacturer's data focusing on an optimized method that would result in reduced computational efforts to merit its use as an engineering design tool.

2. Methodology

2.1. The Numerical Model

This paper focuses on the performance prediction and evaluation of cavitation and pressure pulsation in a commercial DV-H series pump whose specifications are listed in Table 1. To protect proprietary information, only the basic data about the pump (i.e., performance curves and ratings) will be presented in this paper. The DV-H series pump is a single-stage double-suction double-volute axial (horizontal) split case pump suited for high-flow and high-head applications. These types of pumps are designed with between-bearing rotors, as shown in Figure 1, and are classified as the BB1 type under the ANSI/HI 14.3 [15].

For the numerical model, the computational domain includes the active components, the impeller, and the suction and discharge volutes, as shown in Figure 2. The leakage flow paths, balancing holes and wear rings are intentionally omitted because of (1) the unavailability of data and dimensions and (2) the inclusion of these parts is planned for succeeding future studies. Since losses due to these features are neglected in the geometry, an overestimation of the head is expected during the numerical simulation. To reduce computational time, and since, by design, the impeller blades are in-line, a decision was made to use a symmetrical model utilizing half of the pump and applying the necessary boundary conditions at the plane of symmetry. The inlet and the discharge portion of the domain had been extended to approximately 6 times the diameter. This is to ensure that flows are fully developed as the fluid enters and leaves the pump. It is important to note that this value is arbitrary. Depending on the application and modeling scheme, a shorter extension length (especially for the inlet pipe) may be applied without significantly affecting the results.

Table 1. Pump Specifications.

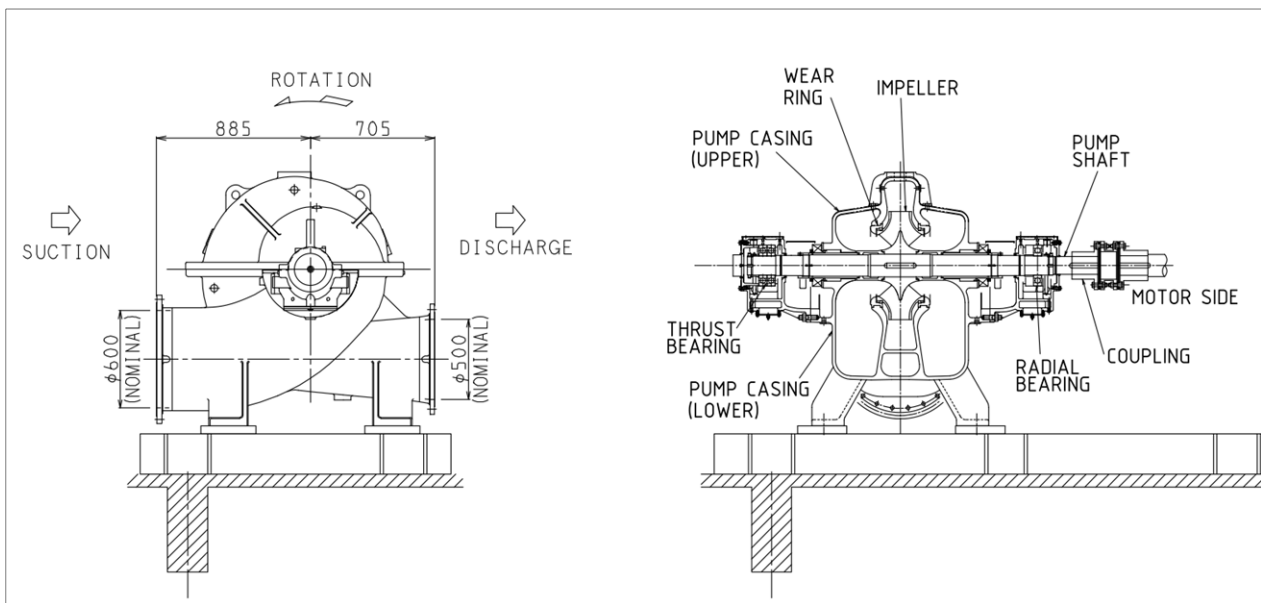| Specification	Value
Type Form	DV-H
Inlet Flange Diameter (m)	0.6
Discharge Flange Diameter (m)	0.5
Stages	single
Capacity (m^3/h)	3620
Total Dynamic Head (m)	91
NPSHa (m)	13
Speed (rpm)	1180
Driver Type	motor-driven
Driver Rating (kW)	2000
Design Efficiency (%)	85
Service	CWP

Figure 1. General arrangement drawing of a double-volute double-suction centrifugal pump.
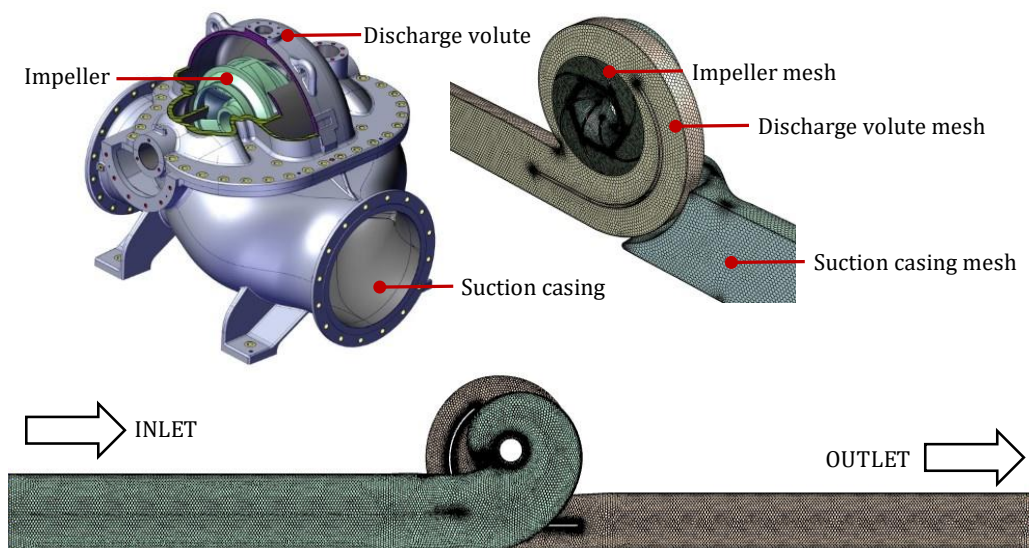

Figure 2. Overview of the numerical domain.

2.2. Solution Setup and Boundary Conditions

All simulation within this paper uses water with properties at normal temperature as the working fluid. The impeller is kept at a constant speed of 1180 RPM. The pump suction is assigned with a pressure inlet boundary condition with flow normal to the boundary, while the pump outlet is assigned a fixed mass flow rate required for the respective analysis. Inlet turbulence condition is assigned an intensity of 5% and a characteristic length equivalent to the pipe inlet diameter. To model the rotor-stator interaction, the MRF approach is used for steady-state solutions, while the sliding mesh approach is used for all transient simulations. The MRF model treats an unsteady problem (with respect to the absolute reference frame) as a steady-state problem with respect to the moving reference frame. Although this approach is an approximation of steady-state conditions, the MRF model simplifies the problem and consequently requires less time and computational effort. On the other hand, the sliding mesh approach in Fluent employs rigid body motion by moving the rotating component at a fixed displacement per time step. Although computationally expensive, especially for large meshes, this method is the most accurate

approach to simulate impeller rotation. To maintain consistency and accuracy, a pressure-based fully coupled algorithm is employed together with a high-resolution upwind scheme for both steady and unsteady equations.

For the unsteady Reynolds-averaged Navier–Stokes (URANS) equations, a time step of $\Delta t = 7.06215 \times 10^{-5}$ seconds resulting in 0.5° of rotation per time step is used. Prior work centered around similar applications has shown that such a time step is sufficiently small for good simulation convergence [16–18]. The simulation is run for a total of ten (10) complete impeller rotations using the pressure distribution from a converged steady-state RANS simulation as initial conditions. The turbulence effect is modeled using a Realizable k-ε scheme applying scalable wall functions for mesh regions with $y^+ > 30$, while assuming the viscous sublayer is properly resolved for regions with $y^+ < 30$. For centrifugal pumps, the Realizable k-ε had been known to reflect better agreement with pump test data as compared to the other 2 k-ε models (i.e., RNG and standard) [19]. In Fluent, the extra rotation term used by this turbulence model in calculating the mean rate-of-rotation tensor is, by default, inactive, making the Realizable k-ε applicable for MRF and sliding mesh applications [20]. The convergence criterion, defined as the root-mean-square residual for all equations at the end of each time step, is set below 1×10^{-5}. Using an Intel i7-9700k CPU with 64 GB of RAM CPU, convergence for each timestep was constantly achieved between 15–20 iteration loops with one (1) impeller rotation being completed in approximately 30 h.

2.3. NPSH Calculation Procedure

Traditional NPSH calculation procedures usually incorporate a trial-and-error approach in determining the pump's NPSH3, which is defined as the suction head that will cause a 3% decrease in the pump's total dynamic head. Such a procedure is tedious and often requires multiple simulations, especially if no information about the pump's NPSHr range is available. Simulations can result in a long convergence time, especially if the flow undergoes severe cavitation. To speed up NPSH prediction, the novel procedure developed by Ding et al. [14] was used in this paper. The procedure involves applying a new set of boundary conditions to the numerical model and using an algorithm to estimate a required outlet pressure that would cause a 3% drop in the pump head. The procedure is both controllable and predictable, which results in determining NPSH yielding a 3.3% head drop in just 3 simulation steps [21]. Figure 3 illustrates the procedure for calculating NPSH3 using the mentioned approach.

2.4. Cavitation Prediction

To model the cavitation phenomena, the Zwart–Gerber–Belamri [ZGB] [22] model was used for the analysis. Since cavitation basically involves a phase change from liquid to gas, the ZGB model is implemented in Fluent as an interphase mass transfer process. Similar to other cavitation models, ZGB is a simplification of the Rayleigh-Plesset equation [23] and assumes a constant nucleation site volume. It is robust and has already been validated in several studies for the prediction of sheet cavitation around hydrofoils [24,25], centrifugal pumps [26], marine propellers and Kaplan turbines [27]. In addition, ZGB is the most compatible model for the turbulence models within Fluent [20]. To complete the cavitation analysis, the working model is changed from a single-phase liquid to a multiphase mixture with water vapor ($\rho = 0.5542$ kg/m^3) as the secondary phase and liquid water ($\rho = 998.2$ kg/m^3) as the primary phase. To obtain a converged solution, the single-phase, steady-state, non-cavitating liquid flow is computed first to achieve a realistic pressure field, then the cavitation model is enabled. The vaporization pressure and bubble radius size were set to 3574 Pa and 1 μm, respectively.
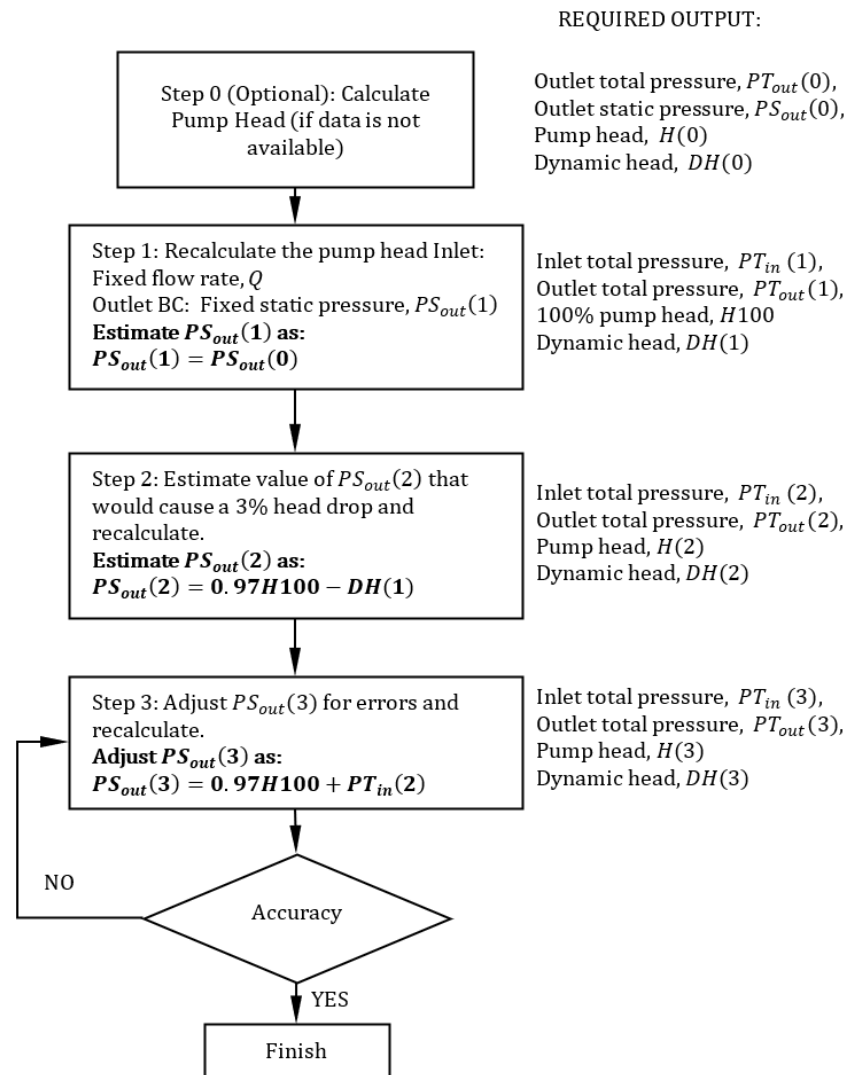
REQUIRED OUTPUT:

| Step 0 (Optional): Calculate Pump Head (if data is not available) | Outlet total pressure, $PT_{out}(0)$, Outlet static pressure, $PS_{out}(0)$, Pump head, $H(0)$ Dynamic head, $DH(0)$ |

Step 1: Recalculate the pump head Inlet:
Fixed flow rate, Q
Outlet BC: Fixed static pressure, $PS_{out}(1)$
Estimate $PS_{out}(1)$ as:
$PS_{out}(1) = PS_{out}(0)$

Inlet total pressure, $PT_{in}(1)$,
Outlet total pressure, $PT_{out}(1)$,
100% pump head, $H100$
Dynamic head, $DH(1)$

Step 2: Estimate value of $PS_{out}(2)$ that would cause a 3% head drop and recalculate.
Estimate $PS_{out}(2)$ as:
$PS_{out}(2) = 0.97H100 - DH(1)$

Inlet total pressure, $PT_{in}(2)$,
Outlet total pressure, $PT_{out}(2)$,
Pump head, $H(2)$
Dynamic head, $DH(2)$

Step 3: Adjust $PS_{out}(3)$ for errors and recalculate.
Adjust $PS_{out}(3)$ as:
$PS_{out}(3) = 0.97H100 + PT_{in}(2)$

Inlet total pressure, $PT_{in}(3)$,
Outlet total pressure, $PT_{out}(3)$,
Pump head, $H(3)$
Dynamic head, $DH(3)$

NO

Accuracy

YES

Finish

Figure 3. Procedure for calculating NPHR3 as proposed by Ding et al. [14].

2.5. Pressure Fluctuations

To study the pressure fluctuations caused by the hydraulic interaction between the rotating impeller and the stationary volute casing, the unsteady analysis is run for ten rotations at 100% rated flow. Since it is expected that pressure variation will be highest near the cutwaters and near the topside of the casing wall, data is collected from monitoring points located in the volute, as shown in Figure 4. Pressure fluctuation data for the three (3) points are collected and normalized into a nondimensional pressure coefficient, c_p, defined as:

$$c_p = \frac{p - \bar{p}}{0.5\rho\mu_2^2} \tag{1}$$

where p and $\bar{p}$ represent the unsteady pressure and the average pressure at each monitoring point, respectively. μ_2 is the impeller outlet tip speed, and ρ, is the fluid density.
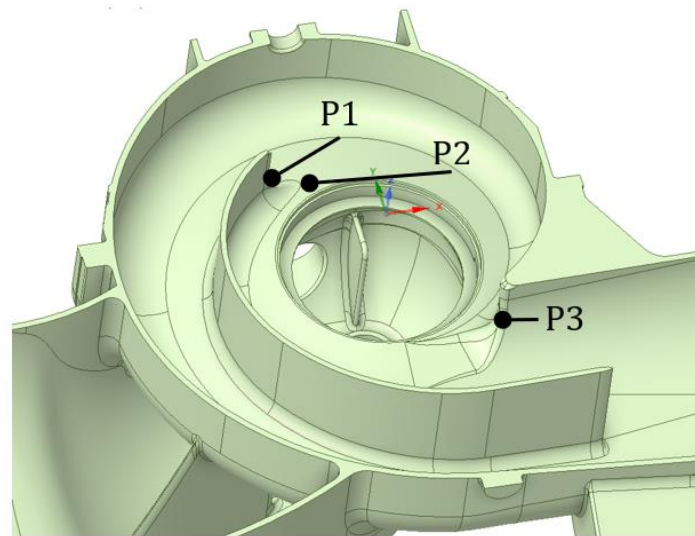
Figure 4. Location of monitoring points for the volute casing.

2.6. Grid Generation and Grid Independence Study

Grids for the CFD domain were prepared using the new Poly-Hexcore Mosaic meshing technology developed by ANSYS, as shown in Figure 5. Compared to a similarly sized multi-block structured hexagonal model, applying the Poly-Hexcore Mosaic mesh technique to the pump in this study resulted in ~37% fewer cells. Fluent's Poly-Hexcore Mosaic meshing technology also incorporates parallel volume meshing capability, which, combined with the lower resulting cell counts, aids in decreasing mesh creation time.
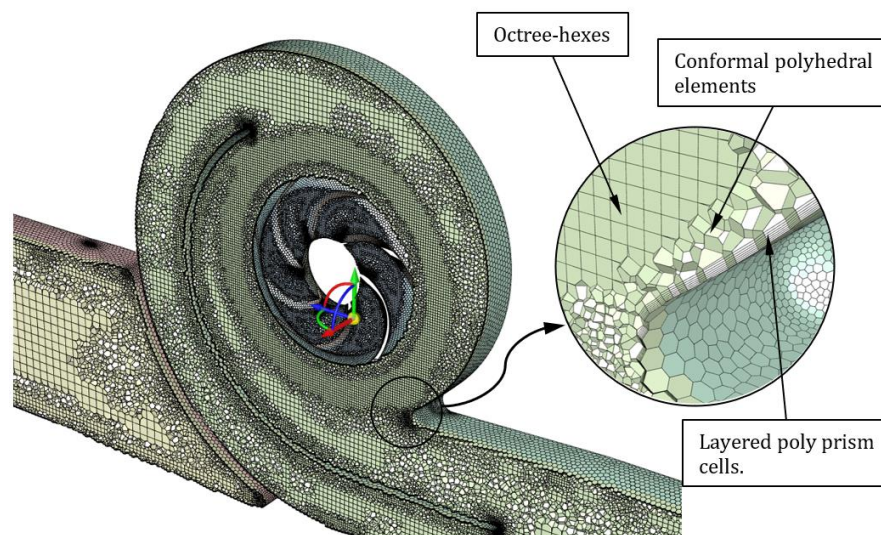
Figure 5. Clipped view of mosaic mesh generated using ANSYS Fluent Mosaic mesh technology.

The computational domain was divided into three regions: the suction casing, the rotating impeller, and the discharge volute. The three regions are connected using internal interface boundary conditions as employed within Fluent. To achieve a reasonable number of grid elements, the discharge volute and impeller regions were modeled with high-density mesh since these areas are expected to have a high solution gradient, while the suction volute, inlet, and outlet sections are modeled with lower-density mesh counts since flow within these areas is of no particular interest to the study. To ensure that the results are grid-independent, several models with varying mesh densities were created, as shown in Table 2. A single-phase steady-state solution is then executed with the pump running at

the design flow of 3620 m^3/h and a fixed rotational speed of 1180 RPM. The results of the pump's external performance parameters are then tabulated and compared to check the effect of grid density on the solution.

Table 2. Mesh domain for grid sensitivity analysis.

	Mesh 1	**Mesh 2**	**Mesh 3**	**Mesh 4**	**Mesh 5**	**Mesh 6**	**Mesh 7**
Suction Casing	275,321	320,162	398,708	594,525	522,420	832,840	998,808
Impeller	528,863	581,358	683,105	1,074,400	1,385,464	1,434,188	1,477,963
Discharge Volute	171,022	247,721	339,951	522,420	594,525	969,173	1,269,143
Total No. of Cells	975,206	1,149,241	1,421,764	2,191,345	2,502,409	3,236,201	3,745,914

Figure 6 shows the head and efficiency as derived from the numerical results for all grid sizes. These results show that, by taking the results for Mesh 7 as the baseline, all numerical models with cell counts above 2×10^6 predicted the head and efficiency well within 1% of the baseline. Conversely, significant deviations can be seen in the calculated values for the models with lower numbers of cells. Considering speed and accuracy, the model with 2,191,345 elements, Mesh 4, was used for succeeding analyses. Figure 7 shows the y^+ distribution across the blade surface for Mesh 4. The average y^+ for this mesh is 78 while the maximum value is 245.
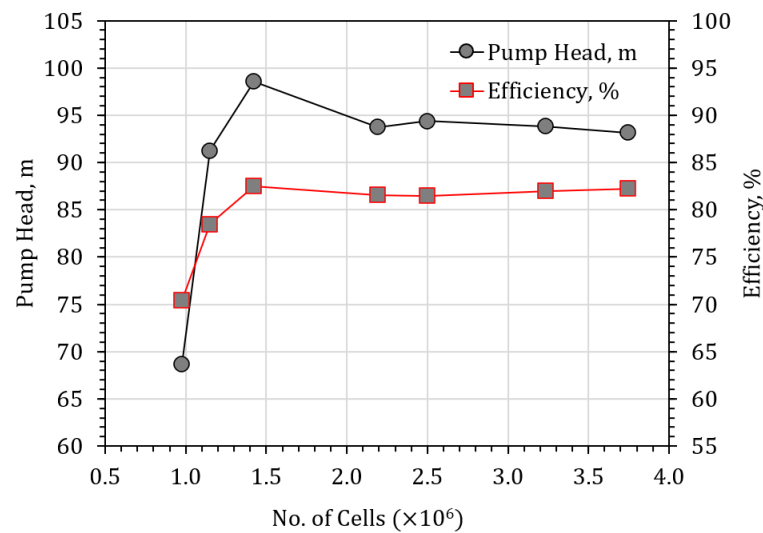

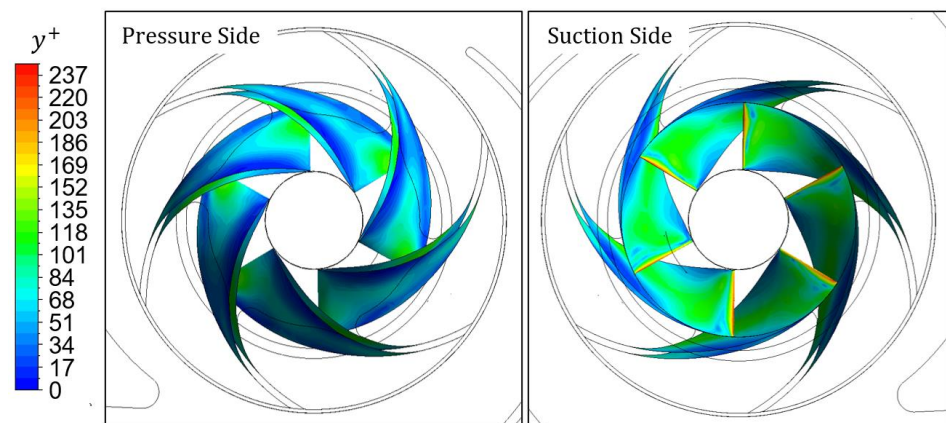**Figure 6.** Pump head and efficiency results from grid sensitivity analysis.

Figure 7. Contour plot of the y^+ distribution on the blade's surface.

3. Results and Discussions

3.1. Validation Using Pump Performance Data

To validate the accuracy of the selected domain and turbulence model, performance data for various flow conditions were collected from non-cavitating single-phase transient simulations for flow ranges between 20–120% of the rated flow rate. These data are then compared to the expected pump characteristic curve as provided by the manufacturer. For the performance parameters, the pump head, shaft power, and efficiency were calculated as follows:

$$\text{Head} : H = \frac{P_{out}}{\rho g} - \frac{P_{in}}{\rho g} + \Delta z \tag{2}$$

$$\text{Shaft Power} : P = T \times \omega \tag{3}$$

$$\text{Efficiency} : \eta = \frac{\rho g Q H}{P} \tag{4}$$

where in P_{in} and P_{out} are the mass-weighted average of the total pressure taken at the pipe inlet and outlet flanges, respectively, g is the acceleration due to gravity, ρ is the fluid density, T is the torque, ω is the angular velocity, and Q is the fluid flow rate. Since the inlet and outlet flanges are at the same elevation, Δz for this pump is taken as 0.

Figure 8 shows the comparison between numerical results and the pump manufacturer's expected performance curve. It can be seen from the figure that the head, efficiency, and shaft power for Mesh 4 at various flow conditions follow a consistent trend and closely matches the data provided by the manufacturer. The simulation results at the rated flow of 3620 m^3/h show a head of 93.7 m and an efficiency of 81.5%. The pump head is overestimated by 3%, which is as expected since leakage losses were neglected because geometries like the wear ring and leakage flow paths were omitted from the numerical model for simplification. The graph also shows that the pump's rated flow is at ~83% of the best efficiency point (BEP), which, as per ANSI/HI standards [28], is well within the preferred operating range (POR = 70−120% of BEP) for this type of pump. These results indicate that the model selection, choice of turbulence models, as well as solution schemes, are sufficient for this study.
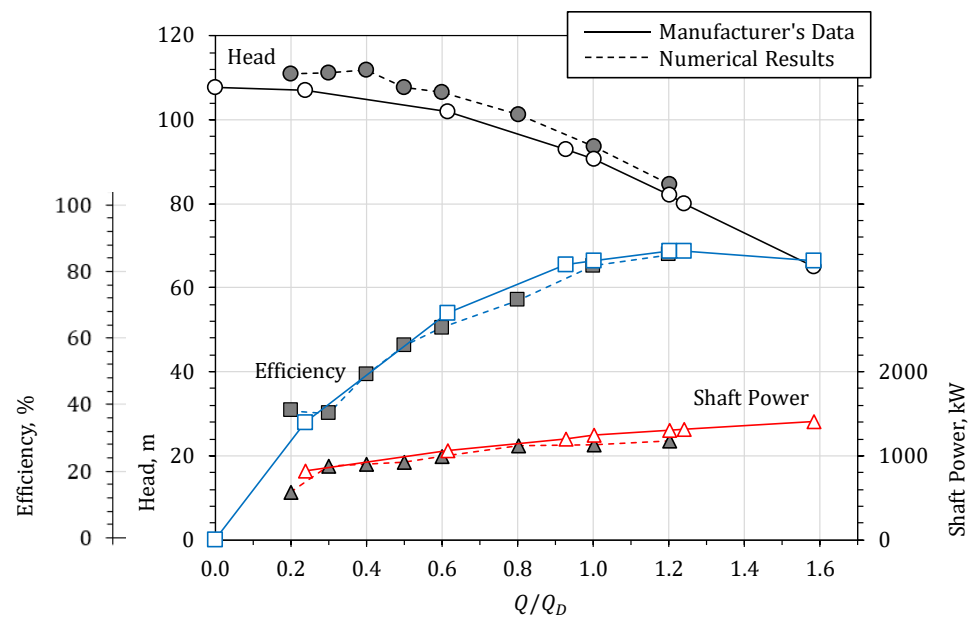

Figure 8. Pump Performance Curve based on CFD calculations and Manufacturer's data.

3.2. Comparison between Poly-Hexcore Mesh and Multi-Block Structured Hexagonal Mesh Model

To further verify the results obtained with the Poly-Hexcore mesh, a similar geometry with a multi-block structured hexagonal mesh (Figure 9) was prepared using an in-house mesh generation software. Because the meshing process was not completely automatic,

preparing the mesh took a total of ~17 h to complete. This is in contrast with the fully automatic capability in preparing the Poly-Hexcore mesh, which was able to prepare the mesh within ~30 min using an Intel i7-9700k CPU with 64GB of RAM.
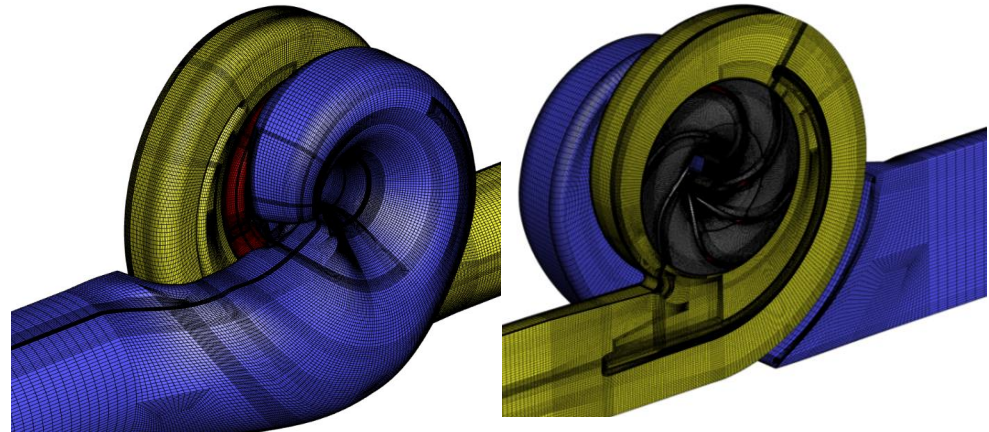

Figure 9. Multi-block structured hexagonal mesh of double-volute double-suction pump.

To minimize variations due to element sizing, the multi-block structured mesh model was subdivided into four regions, and a global element size close to that of the Poly-Hexcore mesh was adopted. The mesh structure, as well as a comparison of the mesh density and quality of the two models, is shown in Figure 10. From the figure, it can be seen that the model with the Poly-Hexcore mesh has a substantial advantage in terms of mesh quality over the structured model. This is understandable since the bulk of the model is meshed using octree-hexes.
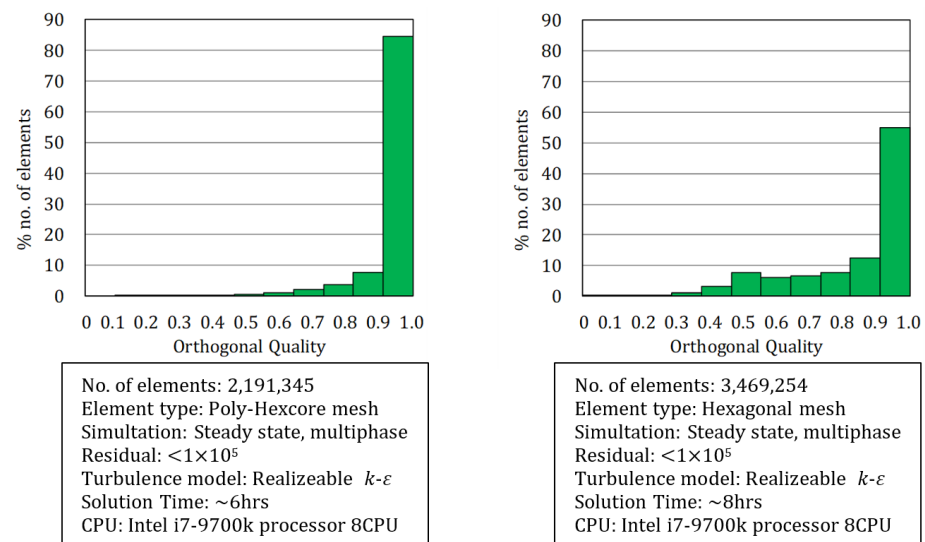

No. of elements: 2,191,345
Element type: Poly-Hexcore mesh
Simulation: Steady state, multiphase
Residual: <1×10⁵
Turbulence model: Realizeable k-ε
Solution Time: ~6hrs
CPU: Intel i7-9700k processor 8CPU

No. of elements: 3,469,254
Element type: Hexagonal mesh
Simulation: Steady state, multiphase
Residual: <1×10⁵
Turbulence model: Realizeable k-ε
Solution Time: ~8hrs
CPU: Intel i7-9700k processor 8CPU

Figure 10. Element quality distribution for Poly-Hexcore and Hexagonal mesh models.

Calculations were run on both models at the rated flow to check for pump performance. The Poly Hexcore Mesh reflected values for head and efficiency as 93.7 m and 81.5%, respectively. These results are acceptably close to the values calculated using the hexagonal mesh, which are 94.6 m and 80.2%. The steady-state calculation time for the Poly-Hexcore was around ~25% shorter compared to the other model, which is a significant reduction. Additionally, from the plots of the contours for both models (Figure 11), it can be seen that the pressure and velocity distribution between the two are fairly similar, signifying that the accuracy of the model with the Poly-Hexcore mesh is equally accurate when compared to the structured mesh model.
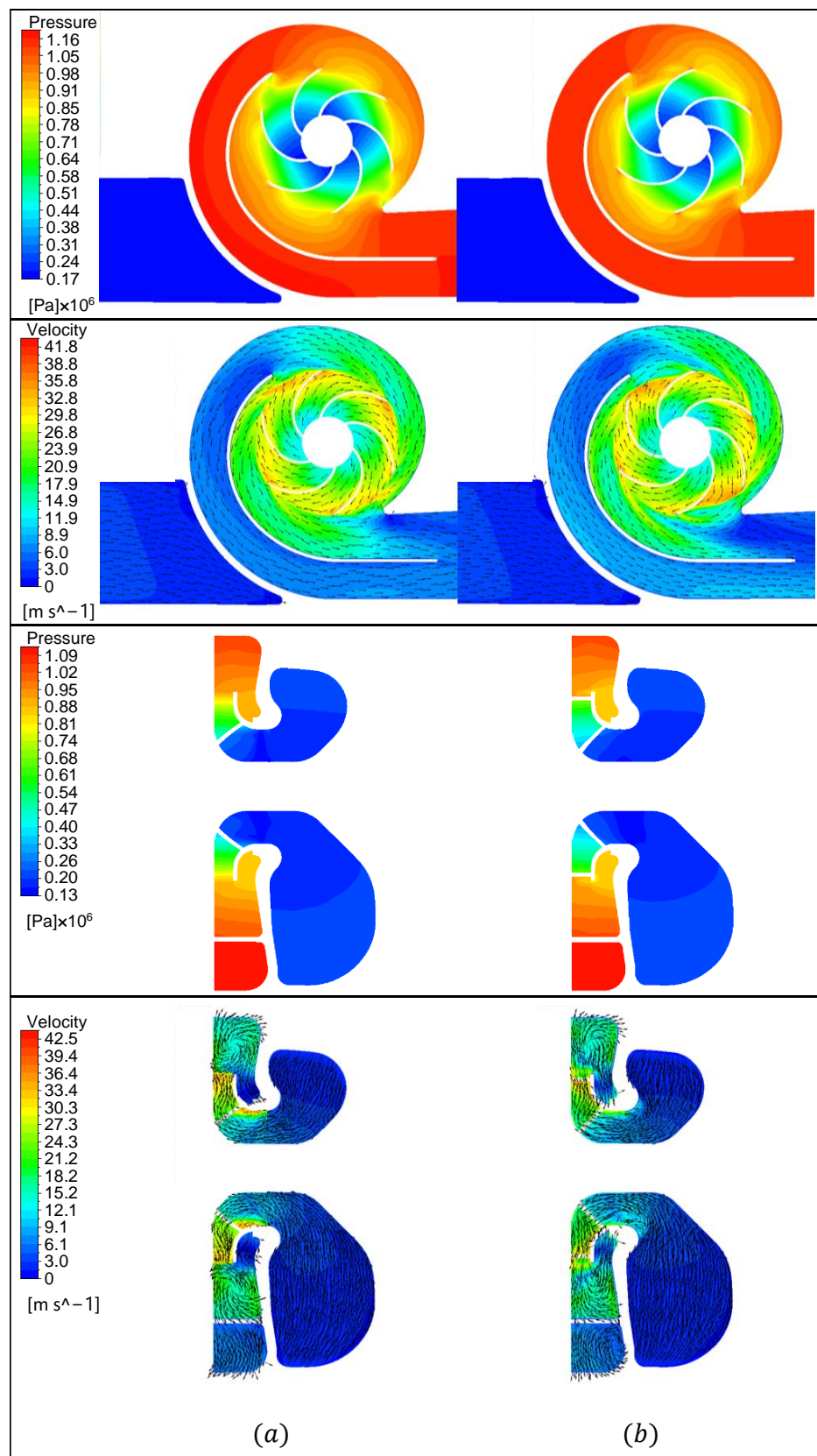
Figure 11. Pressure and velocity contour plots at rated flow for (**a**) the model with Poly-Hexcore Mesh and (**b**) the model with multi-block structured hexagonal mesh.

3.3. Flow Pattern and Pressure Distribution for Non-Cavitating Condition

To have a better perspective of the flow within the impeller blades, the blade-to-blade view of the static pressure is shown in Figure 12. The views, taken at midspan between hub and shroud, represent results for flowrates equivalent to 80%, 100%, and 120% of the rated flow, Q_D. Similarly, the velocity streamlines plotted at a cross-section cutting across the impeller at a 20% constant span between the hub and shroud are shown in Figure 13. From these figures (Figure 13b,c), the streamlines are perfectly aligned with the blade profile developing a smooth distribution along the impeller for both Q_D and 1.2Q_D. However, from the pressure plots (Figure 12b,c) of the mentioned flow rates, it is apparent that the leading edge of the blades tends to act as an obstruction for incoming flow resulting in an area with low static pressure on both sides of the blades. This shows that even at the best efficiency point (1.2Q_D), cavitation can still take place once there is a significant drop in the inlet pressure. Specifically, for the pump in this study, it can be assumed, based on the same figures, that due to the lower static pressure, cavitation will most likely start to form as thin sheets of vapor on the suction side of the leading edge of the blade. On the contrary, for flow equivalent to 0.8Q_D, since this flow is outside of the pump's POR, significant nonuniformity can be seen in the velocity streamlines (Figure 13a). Flow is turning towards the pressure side creating flow distortions and several axial vortices between the impeller blades. This phenomenon, termed recirculation, primarily occurs during part-load conditions (sometimes starting as high as 70% of Q_{BEP}). In the recirculating region, the same volume of fluid is being acted upon by the impeller imparting additional energy to the fluid. This can contribute to higher heads compared to non-circulating flows. This phenomenon may seem beneficial for other pumps (e.g., regenerative pumps), but for the centrifugal pump in this study, this increase in the head caused by recirculation is meaningless since these types of pumps cannot operate in this flow condition. Also, again at part-load (0.8Q_D), the blade-to-blade plot (Figure 12a). reveals that there is a larger low-pressure area at the suction side of the impeller for this flow rate as compared to the previous two cases. Although the plot shows only the pressure distribution at mid-span, by combining this information with the knowledge of the flow profile as derived from Figure 13a, it can be approximated that this low-pressure region extends across the surface of the blade in the spanwise direction. Consequently, this low-pressure area can lead to cavitation, which can ultimately damage the impeller and create undue stress on the rotor components due to unbalanced forces.

3.4. Predicting Required Net Positive Suction Head (NPSH)

The Hydraulic Institute [29] defines the NPSHr of a pump as the minimum NPSH given by the manufacturer/supplier for a pump to achieve a specified performance at the specified rate of flow, rotational speed, and pumped liquid. A common misconception that has been diffused among pump users, designers and even pumped vendors states that NPSHr is a minimum condition that should be observed to guarantee the absence of cavitation. Where this may be true when the standard was first introduced, for modern higher speed, higher density pumps, it should be clearly noted that NPSHr and NPSH3 should have always been linked together, and under such conditions, cavitation is already fully developed hence resulting in a drop of the head. NPSH3 signals that the pump is already affected by cavitation. For practical purposes, the definition widely accepted across the pump industry is that NPSH3 is the NPSH that will cause a 3% drop in the total head (first-stage head for a multistage pump) due to cavitation and that operating the pump at or near this level will certainly cause severe damage and unacceptable service life.
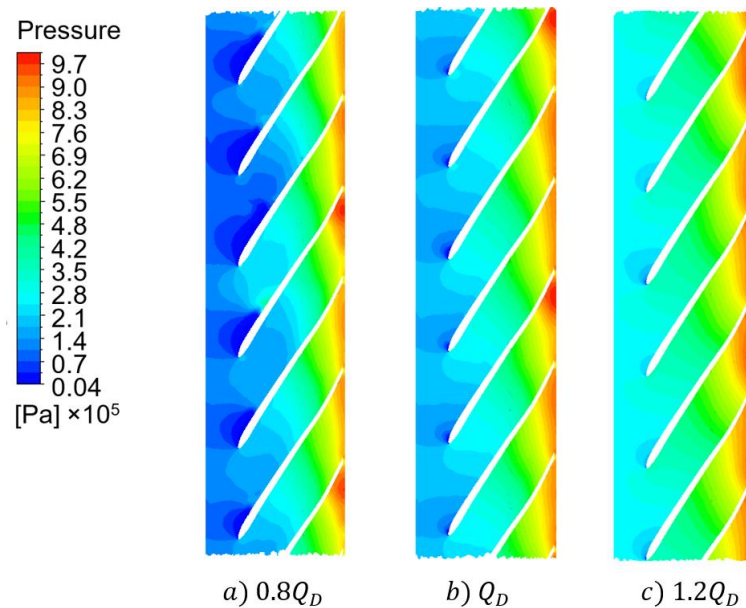
a) $0.8Q_D$ b) Q_D c) $1.2Q_D$

Figure 12. Pressure contour plots on blade-to-blade surface taken at midspan at various flow rates: (**a**) 80% *rated flow*, Q_D, (**b**) *rated flow*, Q_D, (**c**) 120% *rated flow*, Q_D.
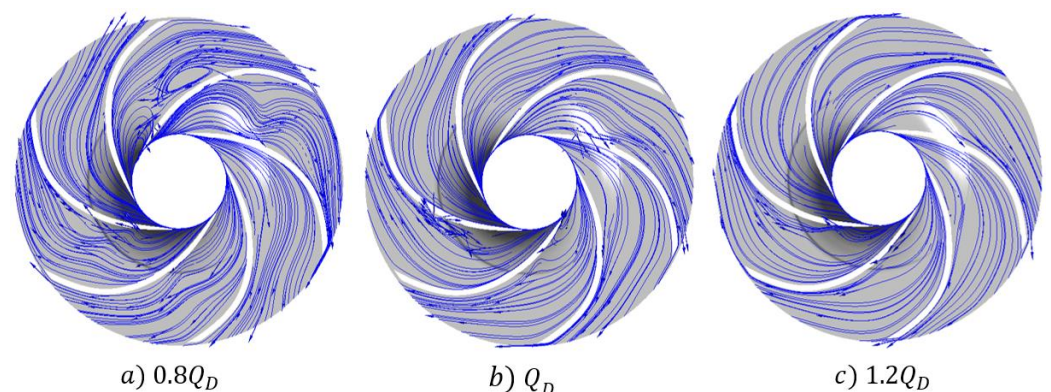

a) $0.8Q_D$ b) Q_D c) $1.2Q_D$

Figure 13. Velocity streamlines on the surface at a 20% constant span between the impeller hub and shroud at various flow rates: (**a**) 80% *rated flow*, Q_D, (**b**) *rated flow*, Q_D, (**c**) 120% *rated flow*, Q_D.

Figure 14 shows the head drop curve and NPSH curve for the DV-H pump for three flow rates as calculated in Fluent using the procedure discussed earlier. Through this approach, the NPSH3 for $0.8Q_D$, $100Q_D$, and $1.2Q_D$ were identified using only 3 to 4 simulations steps. This is a significant improvement as compared to calculating NPSH using the traditional procedure of gradually reducing the inlet pressure during the analysis until a 3% head drop is observed. Comparing the results with the data supplied by the manufacturer, the simulation results showed that at rated flow, Q_D, an NPSH of 5.2 m produced a 3.05% drop in the total head. This result is relatively close to the expected 5.7 m NPSH3 value from the pump manufacturer's NPSH curve. However, while still in Figure 14, the noticeable increase in the discrepancy between the calculated NPSH3 value and the data supplied by the manufacturer as the flow decreases should not be considered as an inaccuracy in the numerical model. Instead, it should be noted that the NPSH3 calculations in this paper were executed for 3–4 steps only for each flow rate resulting in a ~3.05% head drop. Additional iteration is expected to increase the calculated NPSH3 value as the head drop reaches 3% and thus reducing the gap between the two data sets. Although in this paper, this is deemed unnecessary since, in general, the predicted values

are within acceptable limits and prove that the greater suction area inherent in the design of these types of pumps is advantageous in installations where the available NPSH is limited.
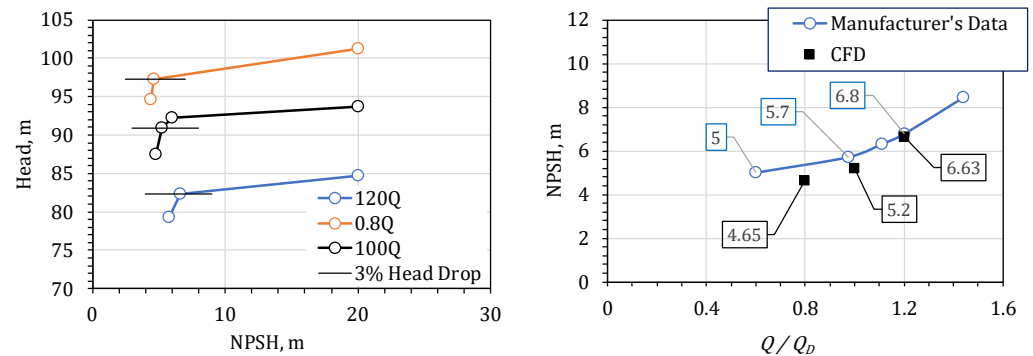

Figure 14. NPSH values, as predicted using a novel approach [14]. (**Left**) head-drop curve. (**Right**) NPSH characteristic curve.

3.5. Cavitation Growth

To further visualize the cavitation phenomenon in the pump, plots of the void fraction iso-surface for the void cavity corresponding to $\alpha = 10\%$ for the tested flow condition are presented below. These iso-surface plots approximate the location and size of the cavity developed as the available NPSH is decreased. At rated flow, Q_D, it can be seen from Figure 15 that cavitation tends to start on the suction side of the blade when the inlet pressure is gradually reduced. This verifies the assumption made in Section 3.3 when observing the pressure contour plots on the blades.
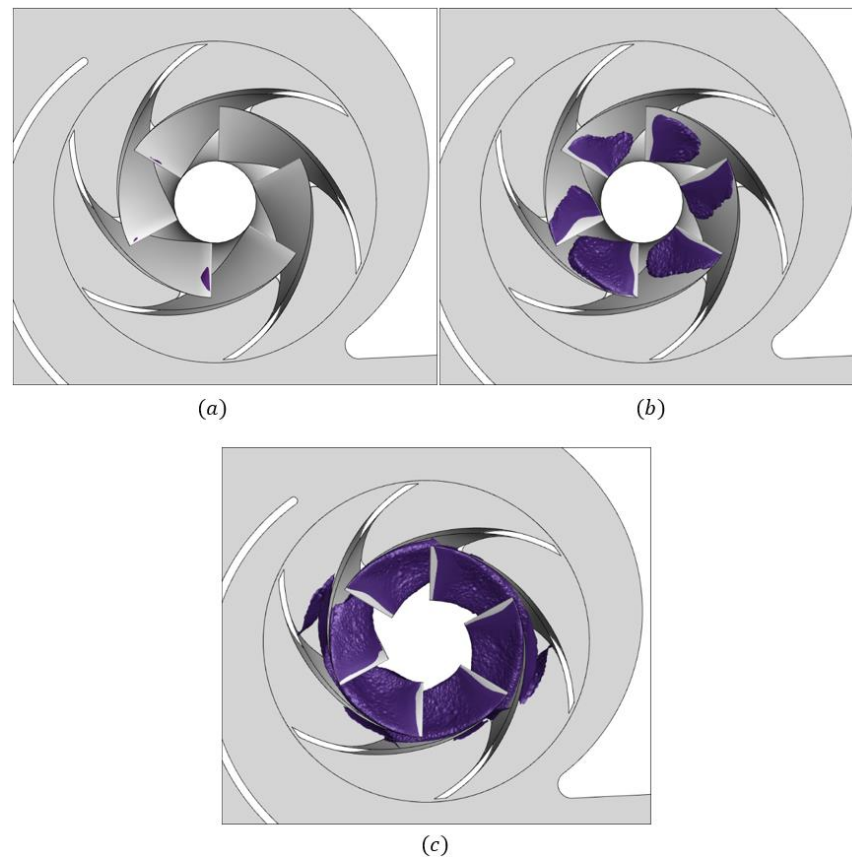

Figure 15. Iso-surface plot of volume fraction ($\alpha = 0.1$) at rated flow Q_D: (**a**) $NPSH = 20$ m, (**b**) $NPSH = 5.9$ m, (**c**) $NPSH3$.

In Figure 15a, at NPSH = 20 m, cavitation bubbles on the leading edge of the blade near the hub can already be observed. The formation of the cavity bubble on the suction side is as expected since the rated flow for this pump is considered as part load as compared to the flow at the best efficiency point. This is in contrast with running the pump condition above Q_{BEP}. At overload condition, cavitation starts to form on the pressure side of the blade because of the lower pressure in that region. Looking back at the figure, it can be seen that the cavity continues to grow as the suction pressure is reduced. Figure 15b shows the formation of a noticeably sized cavity near the leading edge with minimal effect (~1.5%) on the pump head. This means that even before reaching the NPSH3 level, there is already a significant amount of cavitation. As such, it is important to add a relevant NPSH margin ($\geq$+0.5 m) when stating the specifications for this pump. At NPSH3, the cavity continues to expand while the head continues to drop significantly (Figure 15c). It is very difficult to provide a more accurate description since bubble geometry and its damaging effect are influenced by numerous factors. Chief amongst them are impeller material, inlet and blade geometries, water temperature, fluid density, type of cavity, etc. The only guide that designers use is that the absence of visible cavities indicates that cavitation will not be an issue during operation.

3.6. Pressure Variations

3.6.1. Pressure Variations in the Volute Casing

Figure 16 shows pressure contour plots for two blade positions at the rated flow Q_D, specifically (Figure 16a) when the impeller rotates, placing the volute cutwater in between two succeeding blade tips and (Figure 16b) when the trailing edge of the blade is adjacent to the cutwater. From these figures, it can be observed that in Figure 16a, disregarding the minor localized pressure variations near both cutwaters, the pressure gradient across all six blades is relatively uniform. This condition was inspected to be relatively consistent across contours plots of other blade positions near the one presented in the figure. On the other hand, once the impeller is in a position wherein the blade tip is aligned or adjacent to the cutwater, as in Figure 16b, significant pressure variation can be noted. One point of interest is that when the blades are aligned with the cutwater, the pressure distribution on the two sides of the impeller changes in magnitude in a way where the pressure side of the blade is observed to experience a lower pressure than the suction side. These strong pressure gradients are further verified by recording the pressure fluctuations near both cutwaters in the time history domain.
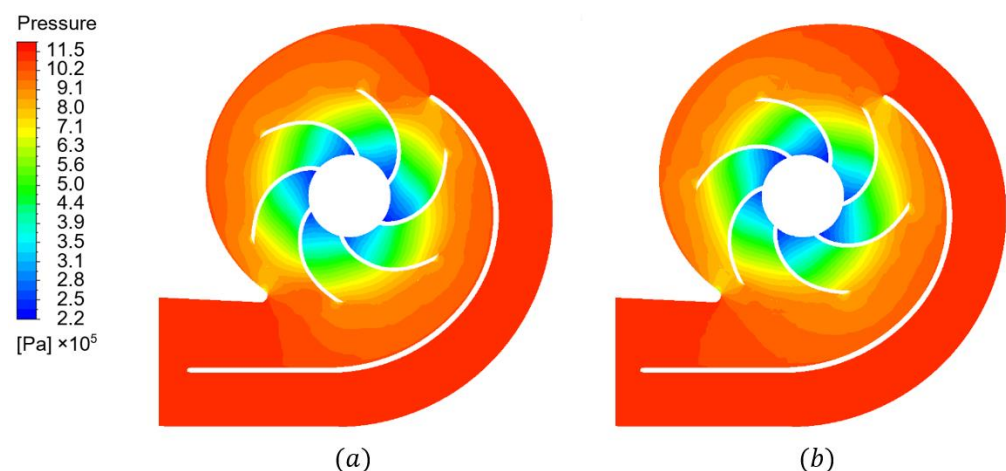

Figure 16. Pressure distribution at midspan between the impeller hub and shroud. (**a**) uniform pressure contour when blades are not aligned with the cutwater. (**b**) pressure side experiencing lower pressure than the suction side on blades aligned with the cutwaters.

Figure 17 shows a time history chart of the pressures on monitoring points $P1$, $P2$, and $P3$. Normalized pressure coefficient, c_p, is plotted against the total time required for one complete impeller rotation. This graph describes the relationship of the pressure variations to the rotation of the impeller relative to the volute. For each monitoring point, the pressure reaches the maximum point as the blade approaches the monitoring point and rapidly drops as the same blade clears this stationary part of the volute. It is at this point that the maximum amount of energy exerted by the fluid is directed toward the discharge nozzle/splitter. The pressure then again rises steadily as the next blade reaches the same position. This periodic pressure fluctuation is represented by the six peaks in the graph. Similar to other hydrodynamic phenomena, such as vortex flow and cavitation, this interaction between the impeller blade and volute casing contributes to pump vibration and noise. It is interesting to note that the figure shows that the monitoring point $P1$ on the splitter cutwater experiences higher pressure fluctuations as compared to the volute cutwater. To avoid this imbalance, it is necessary that both cutwaters are designed to be as similar as possible. However, it is also important to understand that due to the shock loss experienced as the blades pass these cutwaters, a slight difference in pressure variation between these stationary components should be expected.
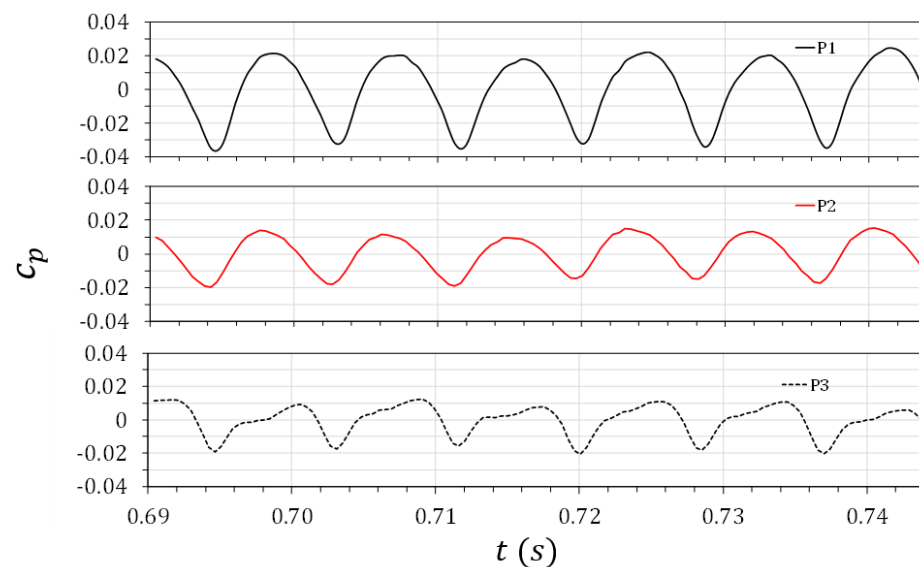

Figure 17. Time history plot of normalized pressure coefficient, c_p, on monitoring points $P1$, $P2$, and $P3$.

Figure 18 represents the frequency spectra of the time-domain pressure signals for the three monitoring points previously discussed. The amplitude is taken as the dimensionless pressure coefficient, c_p, while the frequency range is normalized against the pumps blade passing frequency, $f_{BPF} = 118$ Hz. From this figure, pressure pulsations are seen to be generated at the blade passing frequency and its harmonics. This nonuniform flow behavior can be attributed to the interaction between the rotating impeller blade and the stationary component of the volute casing. In a perfect centrifugal pump, these are the only discrete frequencies that would be generated, but as seen from the figure, several discrete components can also be observed below the blade passing frequency. These pressure pulsations or "flow noise" commonly appearing in the low end of the frequency spectra are usually caused by turbulence in the flow, surface irregularities, or in this case, the formation of a cavitation cloud near the leading edge of the impeller, which periodically separates and travels towards the outlet of the impeller. At normal operating conditions, these discrete frequencies are both normal and random and are not usually harmful. However, operating the pump below NPSH3 usually causes the pulsations at these low frequencies to be more dominant than those equivalent to pulsations occurring near f_{BFP}.
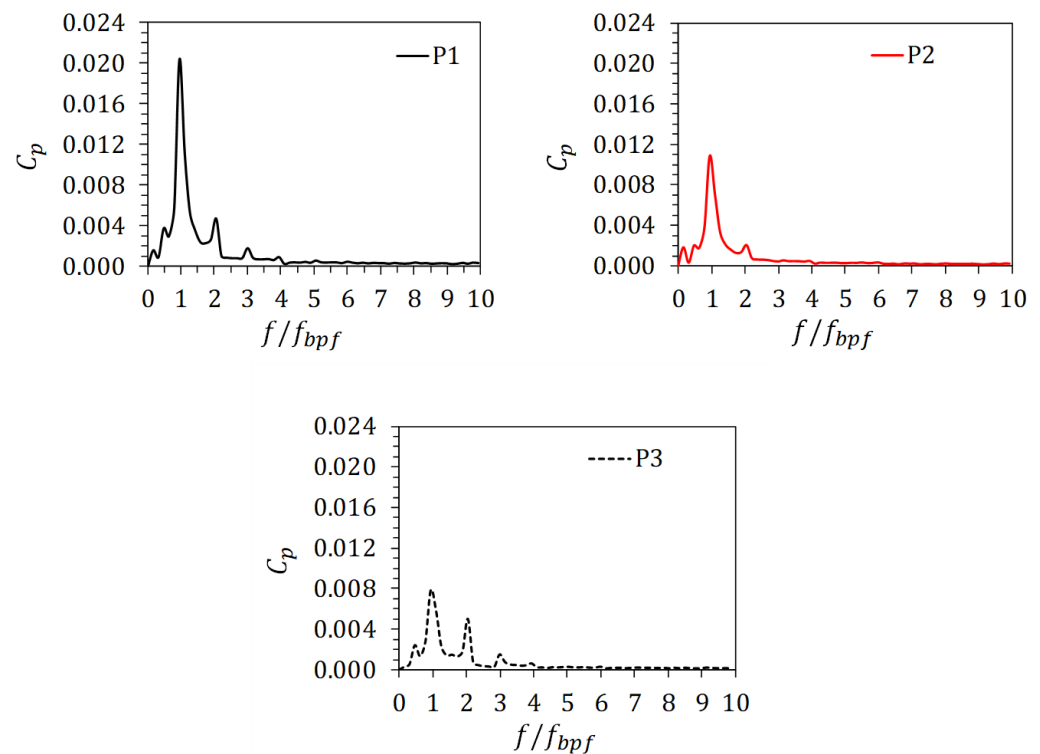
Figure 18. Frequency spectra of the pressure fluctuation on monitoring points *P1*, *P2*, and *P3*.

3.6.2. Pressure Variation on the Impeller Blades

Figure 19 shows the pressure variation at two monitoring points near the trailing edge of the blades. Both points are located at the midspan and are adequately labeled to represent their respective sides of the blade. Again, the graphs represent the normalized pressure coefficient, c_p, collected as the impeller makes one complete revolution. From the figure, it can be observed that the suction side of the blade is experiencing a smaller pressure fluctuation as compared to the pressure side. It also shows that aside from the periodic oscillations like what was seen in the previous section, there are two peaks in the graphs that are 180° apart. These peaks represent the blades' interaction with the diametrically opposed cutwaters. Observation of the flow shows that on the pressure side, these peaks occur just as the blade reaches the cutwater. As the blade travels past the cutwater, the sharp flow variation causes the pump to experience shock loss, represented by the rapid drop in pressure, as the suction side of the blade reaches the same position. In poorly designed pumps, this pressure drop may become large enough to cause the pressure in this region to fall below the fluid's vapor pressure, consequently generating vapor bubbles near the cutwater. As previously mentioned, this rapid bubble formation, growth, and collapse can cause cavitation, and, in this case, the damage will be localized near the cutwater and the impeller blade tip. This localized cavitation damage is known as the passing vane syndrome and is usually caused by the impeller blades passing too close to the cutwater. To avoid this phenomenon, it is important that care must be given in selecting the proper gap between the impeller trailing edge and the volute cutwater during the design stage.
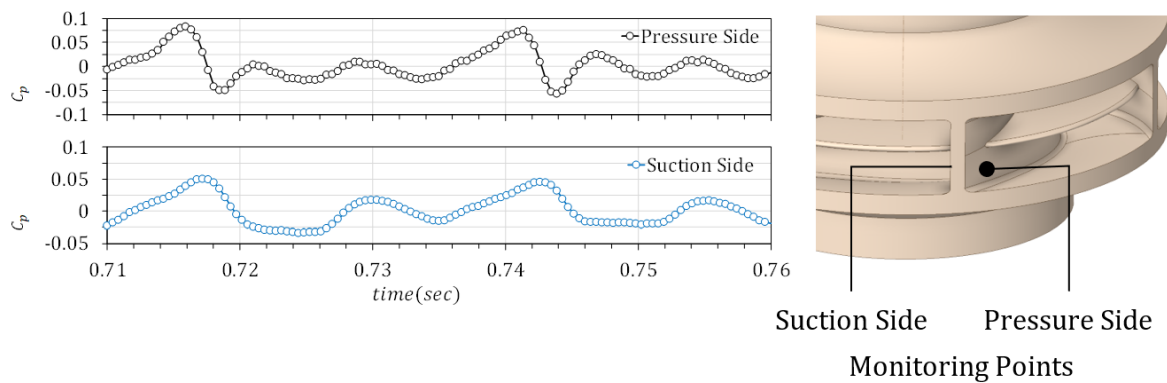
Figure 19. Time history plot of normalized pressure coefficient, c_p, on monitoring points on the blade's surface.

Since the pump in this study is a double-volute pump, the dynamic interaction between the casing and impeller creates two dominant pulses per revolution, one for each cutwater. The weaker pulses recorded on the blade when it is not aligned with the cutwaters can be attributed to the interaction between the other blades with the cutwater. This can be confirmed in the frequency spectra, as shown in Figure 20, where the first dominant frequency is twice that of the shaft frequency. Because of this, it is easy to think that the vane pass frequency for a double-volute pump is simply twice that of a single-volute pump. It is important to note that this is only true for impellers with odd numbers of blades. The pump in this study has six blades, and since the cutwaters are diametrically opposed, for any given angle, two opposite blades generate a pulse at the exact same time. This, therefore, leaves the vane pass frequency unchanged. However, for even-numbered blades, it is expected that the magnitude of the pressure fluctuation will be greater than that of a single-volute pump. As such, it is reasonable to consider odd-numbered blades in designing double-volute pumps to reduce this magnitude.
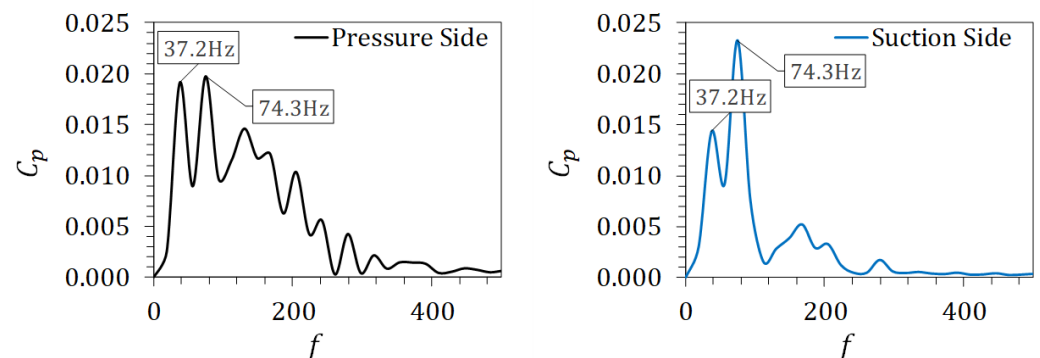

Figure 20. Frequency spectra of the pressure fluctuation on monitoring points on the blade surface.

4. Conclusions

In this paper, numerical analysis results for a double-suction double-volute pump prepared using ANSYS Fluent's Poly-Hexcore meshing technology are presented. CFD simulations were established to predict pump performance as well as other hydraulic phenomena such as cavitation formation, NPSH prediction, and pressure pulsation monitoring. The goal is to lessen the cost of conducting CFD analysis by reducing computational time while maintaining accuracy. As a result, the main conclusions are as follows:

The numerical results for the double-volute double-suction pumps for calculating the performance curve were very close to the data provided by the manufacturer. At Q_D, pump head was over-predicted by 3%, which was expected since leakage flow paths, balancing holes as well as wear rings are intentionally omitted, thereby neglecting leakage losses during the simulation. Comparing the results of the Poly Hexcore mesh model with the

structured hexagonal mesh model showed that values for head and efficiency as 93.7 m and 81.5%, respectively. These results are acceptably close to the values calculated using the hexagonal mesh, which are 94.6 m and 80.2%. The steady-state calculation time for the Poly-Hexcore was around ~25% shorter compared to the other model. Additionally, the fully automatic capability of the Poly-Hexcore mesh technique resulted in the mesh generation of the complete domain within ~30 min using the current hardware. This is in contrast to the semi-automatic mesh preparation used for the structured mesh, which required a total time of ~17 h to complete. In terms of the number of cells, the Poly-Hexcore mesh yielded ~37% lesser number of cells at a substantially shorter time as compared to a manually prepared multi-block structured mesh model. It was also observed that the model with the Poly-Hexcore mesh has a substantial advantage in terms of mesh quality over the structured model. This is understandable since the bulk of the model contains octree-hexes.

The flow pattern within the pump showed that as the flow rate was reduced to 0.8 Q_D, velocity streamlines started to turn towards the pressure side creating flow distortions and several axial vortexes between the impeller blades. This verifies the recirculation phenomena experienced by centrifugal pumps during part load conditions which often result in unnecessary head increase at low flow rates. Similarly, pressure contours revealed a larger low-pressure area along the suction side of the blades when operating at part loads. This shows that under part-load conditions, vapor bubbles are likely to start to form on the suction side of the blade and can ultimately lead to cavitation, which creates undue stress on the rotor components. This is further confirmed by observing the cavitation formation at Q_D across different NPSH conditions. The results of cavitation analysis showed that as high as NPSH = 20 m, the onset of vapor bubbles was seen on the leading edge of the blade. This amount of entrainment (~1%) is normally the maximum limit. Further reduction in suction pressure revealed the formation of a noticeably sized cavity near the leading edge with minimal reduction (~1.5%) on the pump head. This means that even before reaching the NPSH3 level, there is already a significant amount of cavitation for this double-volute pump. As such, it is important to add a relevant NPSH margin ($\geq$+0.5 m) when stating the specifications for this pump.

Lastly, pressure fluctuations resulting from the interaction between the rotating impeller and the stationary volute were tabulated, showing peak pulsations equivalent to the blade passing frequency and its harmonics. It was also observed that even though there were two diametrically opposed cutwaters, having an even number of blades maintained the pulsation frequency similar to that of a single-volute pump. Although it must be noted that the magnitude of the pressure fluctuation will be higher since, in contrast to a single-volute pump, two blades would be simultaneously aligned to the cutwaters for each impeller revolution.

References

1. Gülich, J.F. Impact of three-dimensional phenomena on the design of rotodynamic pumps. *Proc. Inst. Mech. Eng. Part C J. Mech. Eng.* **1999**, *213*, 59–70. [CrossRef]
2. Zhang, Q.; Zhou, H.; Gao, Q.; Cui, Z. Analysis of effects of impeller inlet width on the performance of centrifugal pump. *J. Chem. Pharm. Res.* **2014**, *6*, 2078–2081.
3. Luo, X.; Zhang, Y.; Peng, J.; Xu, H.; Yu, W. Impeller inlet geometry effect on performance improvement for centrifugal pumps. *J. Mech. Sci. Technol.* **2008**, *22*, 1971–1976. [CrossRef]
4. Chakraborty, S.; Pandey, K.M.; Roy, B. Numerical analysis on effects of blade number variations on performance of centrifugal pumps with various rotational speeds. *Int. J. Curr. Eng. Technol.* **2012**, *2*, 143–152.
5. Al-Obaidi, A.R. Investigation of effect of pump rotational speed on performance and detection of cavitation within a centrifugal pump using vibration analysis. *Heliyon* **2019**, *5*, e01910. [CrossRef] [PubMed]
6. Wang, Z.; Qian, Z.; Lu, J.; Wu, P. Effects of flow rate and rotational speed on pressure fluctuations in a double-suction centrifugal pump. *Energy* **2019**, *170*, 212–227. [CrossRef]
7. Chen, S.H.; Liave, L.F. The Flow Field Calculations of a Centrifugal Pump with Volute. In *Volume 1: Aircraft Engine; Marine; Turbomachinery; Microturbines and Small Turbomachinery*; American Society of Mechanical Engineers: Orlando, FL, USA, 1997; p. V001T03A007. [CrossRef]
8. Morgut, M.; Nobile, E. Numerical predictions of cavitating flow around model scale propellers by CFD and advanced model calibration. *Int. J. Rotating Mach.* **2012**, *2012*, 1–11. [CrossRef]
9. Liu, H.L.; Liu, D.X.; Wang, Y.; Wu, X.F.; Wang, J. Application of modified k-ω model to predicting cavitating flow in centrifugal pump. *Water Sci. Eng.* **2013**, *6*, 331–339. [CrossRef]
10. Schnerr, G.H.; Sauer, J. Physical and Numerical Modeling of Unsteady Cavitation Dynamics. In Proceedings of the International Conference on Multiphase Flow, New Orleans, LA, USA, 27 May–June 2001; pp. 1–12.
11. Jafarzadeh, B.; Hajari, A.; Alishahi, M.M.; Akbari, M.H. The flow simulation of a low-specific-speed high-speed centrifugal pump. *Appl. Math Model* **2011**, *35*, 242–249. [CrossRef]
12. ANSYS Inc. ANSYS Fluent Mosaic Technology Automatically Combines Disparate Meshes with Polyhedral Elements for Fast, Accurate Flow Resolution. Available online: https://www.ansys.com/content/dam/resource-center/white-paper/ansys-fluent-mosaic-technology-wp.pdf (accessed on 8 September 2022).
13. Zore, K.; Sasanapuri, B.; Parkhi, G.; Varghese, A. ANSYS Mosaic Poly-Hexcore Mesh for High-Lift Aircraft Configuration. In Proceedings of the 21st AeSI Annual CFD Symposium, Bangalore, India, 18–19 August 2019.
14. Ding, H.; Visser, F.C.; Jiang, Y. A Practical Approach to Speed up NPSHr Prediction of Centrifugal Pumps Using CFD Cavitation Model. In *Volume 1: Symposia, Parts A and B*; American Society of Mechanical Engineers: Rio Grande, PR, USA, 2012; pp. 505–514. [CrossRef]
15. *ANSI/HI 14.3—2019*; Rotodynamic Pumps for Design and Applications. American National Standard Institute: Washington, DC, USA, 2019.
16. Lundgreen, R.; Maynes, D.; Gorrell, S.; Oliphant, K. Increasing inducer stability and suction performance with a stability control device. *J. Fluids Eng.* **2019**, *141*, 011204. [CrossRef]
17. Gu, Y.; Pei, J.; Yuan, S.; Wang, W.; Zhang, F.; Wang, P.; Appiah, D.; Liu, Y. Clocking effect of vaned diffuser on hydraulic performance of high-power pump by using the numerical flow loss visualization method. *Energy* **2019**, *170*, 986–997. [CrossRef]
18. Stephen, C.; Yuan, S.; Pei, J.; Cheng, G.X. Numerical flow prediction in inlet pipe of vertical inline pump. *J. Fluids Eng.* **2018**, *140*, 051201. [CrossRef]
19. Xian-hua, L.; Shu-jia, Z.; Bao-lin, Z.; Qing-bo, H. The Study of the k-ε Turbulence Model for Numerical Simulation of Centrifugal Pump. In *2006 7th International Conference on Computer-Aided Industrial Design and Conceptual Design*; IEEE: Hangzhou, China, 2006; pp. 1–5. [CrossRef]
20. ANSYS Inc. *Ansys Fluent Theory Guide*; ANSYS Inc.: Canonsburg, PA, USA, 2018.
21. Wang, W.; Osman, M.K.; Pei, J.; Gan, X.; Yin, T. Artificial neural networks approach for a multi-objective cavitation optimization design in a double-suction centrifugal pump. *Processes* **2019**, *7*, 246. [CrossRef]
22. Zwart, P.; Gerber, A.G.; Belamri, T. A Two-Phase Flow Model for Predicting Cavitation Dynamics. In Proceedings of the 5th International Conference on Multiphase Flow, Yokohama, Japan, 30 May–3 June 2004.
23. Brennen, C.E.; Christopher, E. *Cavitation and Bubble Dynamics*; Oxford University Press: Oxford, UK, 1995.
24. Hidalgo, V.; Luo, X.W.; Escaler, X.; Ji, B.; Aguinaga, A. Implicit large eddy simulation of unsteady cloud cavitation around a plane-convex hydrofoil. *J. Hydrodyn* **2015**, *27*, 815–823. [CrossRef]
25. Morgut, M.; Nobile, E.; Biluš, I. Comparison of mass transfer models for the numerical prediction of sheet cavitation around a hydrofoil. *Int. J. Multiph. Flow* **2011**, *37*, 620–626. [CrossRef]
26. Liu, H.; Wang, J.; Wang, Y.; Zhang, H.; Huang, H. Influence of the empirical coefficients of cavitation model on predicting cavitating flow in the centrifugal pump. *Int. J. Nav. Archit. Ocean. Eng.* **2014**, *6*, 119–131. [CrossRef]
27. Morgut, M.; Jošt, D.; Nobile, E.; Škerlavaj, A. Numerical predictions of the turbulent cavitating flow around a marine propeller and an axial turbine. *J. Phys. Conf. Ser.* **2015**, *656*, 012066. [CrossRef]

28. *ANSI/HI 9.6.3-2017*; Rotodynamic (Centrifugal and Vertical Pumps)—Guidelines for Allowable Operating Regions. American National Standards Institute: Washington, DC, USA, 2017.
29. *ANSI/HI 9.6.1-2012*; Rotodynamic Pumps Guidelines for NPSH Margin. American National Standards Institute: Washington, DC, USA, 2012.